OXFORD

Cerebral Cortex, 2025, **35**, bhaf039
https://doi.org/10.1093/cercor/bhaf039
Advance access publication date 2 March 2025
Original Article

Investigating the complex cortical dynamics of an advanced concentrative absorption meditation called jhanas (ACAM-J): a geometric eigenmode analysis

Ruby M. Potash[1,2], Winson F.Z. Yang[1,2], Brian Winston[3], Selen Atasoy[4,5], Morten L. Kringelbach[4,5,6], Terje Sparby[7,8,9], and Matthew D. Sacchet[1,2,*]

[1]Meditation Research Program, Department of Psychiatry, Massachusetts General Hospital, Harvard Medical School, Boston, MA 02129, United States
[2]Athinoula A. Martinos Center for Biomedical Imaging, Department of Radiology, Massachusetts General Hospital, Harvard Medical School, Boston, MA 02129, United States
[3]Center for Psychedelic and Consciousness Research, Department of Psychiatry and Behavioral Sciences, Johns Hopkins University School of Medicine, Baltimore, MD 21205, United States
[4]Centre for Eudaimonia and Human Flourishing, University of Oxford, Oxford OX3 9BX, United Kingdom
[5]Center of Music in the Brain (MIB), Clinical Medicine, Aarhus University, Aarhus Centrum 8000, Denmark
[6]Department of Psychiatry, University of Oxford, Oxford OX3 7JX, United Kingdom
[7]Department of Philosophy, Steiner University College, 0260 Oslo, Norway
[8]Department of Psychology and Psychotherapy, Witten/Herdecke University, 58448 Witten, Germany
[9]Integrated Curriculum for Anthroposophic Psychology, Witten/Herdecke University, 58448 Witten, Germany
*Corresponding author: Matthew D .Sacchet, Meditation Research Program, Department of Psychiatry, Massachusetts General Hospital, Harvard Medical School, Boston, MA 02129, United States. Email: meditationadministration@mgh.harvard.edu. X: @matthewdsacchet

Advanced meditation has been associated with long- and short-term psychological changes such as bliss, profound insight, and transformation of well-being. However, most advanced meditation neuroimaging analyses have implemented primarily spatially-localized approaches, focusing on discrete regional changes in activity rather than distributed dynamics. The present study uses a geometric eigenmode decomposition of ultrahigh field-strength 7T functional magnetic resonance imaging (fMRI) data from an intensely sampled case study to investigate the complex, distributed cortical dynamics associated with advanced concentrative absorption meditation. Geometric eigenmode decomposition of advanced concentrative absorption meditation and non-meditative control task fMRI data revealed elevated global brain state power and energy patterns of specific advanced concentrative absorption meditation states compared to controls, with mid-frequency spectrum brain state power and energy following a non-random, cubic trajectory through the advanced concentrative absorption meditation sequence. Further, these brain state differences were meaningfully associated with subjective phenomenological reports of attention, intensity of advanced concentrative absorption meditation quality, and sensations. This study unites precise methodological design, a novel fMRI decomposition framework, and rigorous phenomenology to provide valuable insights into the distributed neural signatures of highly refined conscious states. These results underscore similarities and differences between advanced concentrative absorption meditation and other altered states of consciousness like those induced by psychedelics—offering insights into refined conscious states and their implications for health and well-being.

Keywords: 7T fMRI; advanced meditation; consciousness; eigenmode decomposition; neurophenomenology.

Introduction

There is increasing recognition of the well-being and health-related benefits of meditation, sparking interest in unraveling its underlying mechanisms and nuances (Van Dam et al. 2018). While the number of neuroscientific studies of meditation has grown largely in recent years (Tang et al. 2015; Sezer et al. 2022), relatively few studies have examined the neuroscience of "advanced meditation," that is, states and stages of meditation that unfold over time with increasing mastery (Sacchet et al. 2024). We have proposed that advanced states and stages comprise meditative development and trajectories aimed to cultivate long-term psychological changes such as bliss, profound insight, altruistic and compassionate mindsets, and transformation, all toward well-being (Galante et al. 2023; Sacchet et al. 2024), including meditative endpoints associated with profound psychological effects (Chowdhury et al. 2023; Laukkonen et al. 2023; van Lutterveld et al. 2024a). Recent efforts have focused on developing frameworks to systematically study the varying kinds of advanced meditation (e.g. insight, concentration, compassion meditation) including new classification approaches (Sparby and Sacchet 2022) and integration of wisdom traditions (Wright et al. 2023).

One family of advanced meditation is characterized by absorption and concentration; we have classified this group of practices as "advanced concentrative absorption meditation" (ACAM). ACAM has unique, yet commonly shared features across different contemplative traditions (Ernst 1998; Applebaum 2019; Sparby 2019; Fisher 2022), all of which converge on the description of self-induced states characterized by highly stable attention and immense mental absorption. As an advanced meditation practice, jhana meditation (ACAM-J) stands out as an excellent

Received: September 17, 2024. **Revised:** January 31, 2025. **Accepted:** January 31, 2025
© The Author(s) 2025. Published by Oxford University Press. All rights reserved. For permissions, please e-mail: journals.permission@oup.com.

Downloaded from https://academic.oup.com/cercor/article/35/2/bhaf039/8046926 by Harvard Biostatistics user on 04 March 2025

model for studying ACAM (Yang et al. 2024a; Yang et al. 2024b). ACAM-J is comprised of eight phenomenologically rich states that unfold in series, wherein the meditator develops increasingly intense concentration on a meditation object and which can culminate in a momentary cessation of spontaneous mental content (Gunaratana 1988; Sayadaw 2008; Sparby and Sacchet 2024). ACAM-J offers valuable insights into human consciousness as a volitional, sequential development of states that are associated with profound experiences of bliss, calm, clarity, ego dissolution, and open consciousness (Gunaratana 1988; Hagerty et al. 2013; Yamashiro 2015; Dennison 2019; Sparby 2019; Yang et al. 2024a).

ACAM-J states can be broadly organized into (i) the "form" ACAM-J (*rūpa jhanas* from Pāli the liturgical language of Theravada Buddhism), which can be referred to by their numbered states ACAM-J1 to J4, and (ii) "formless" ACAM-J (*arūpa jhānas* or *arūpa āyatanas*), which can be referred to by their primary phenomenological characteristics or numbered states ACAM-J5-J8. ACAM-J are characterized by specific ACAM-J factors, or typical dominant qualities, including directed attention, sustained attention, emotional joy, mental ease, equanimity, and sometimes single-pointedness or one-pointed concentration (Buddhaghosa 2010). The form ACAM-J are marked by a gradual refinement and shift of focus from the form ACAM-J-dominant factors, which diminish until equanimity and single-pointedness remain. While ACAM-J1 to J4 are primarily referenced by their number, the formless ACAM-J—ACAM-J5 to ACAM-J8—are also termed by their qualities known, respectively, as "base of boundless space, base of boundless consciousness, base of nothingness, and base of neither perception nor nonperception." During the formless ACAM-J, consciousness and perception become increasingly highly refined (Catherine 2008; Sayadaw 2008; Rasmussen and Snyder 2009). As meditators advance through the ACAM-J states, they systematically relinquish the dominant qualities of each ACAM-J, allowing them to access increasingly deeper states of consciousness until the final state of ACAM-J8.

The study of ACAM-J provides insight into rich cognitive and phenomenological processes (Sparby and Sacchet 2022; Yang et al. 2024b). Yet, this is a relatively new area of study due to several reasons, including the rarity of adept ACAM-J meditators as well as the rigorous neuroscientific methodology necessary to meaningfully assess these meditative states (Wright et al. 2023). There have been four previous neuroscientific studies of ACAM-J—two using EEG (DeLosAngeles et al. 2016; Dennison 2019), one fMRI and EEG (Hagerty et al. 2013), and one using 7T fMRI with combined phenomenological reports (Yang et al. 2024a). These studies point to the deconstruction of consciousness during ACAM-J; however, studies using fMRI employed region of interest (ROI)-based approaches, which have been limited to univariate regional assessment of activity. Given the distributed nature of higher-level brain function, we instead use a neuroimaging analysis technique that characterizes the large-scale cortical dynamics of these advanced meditative states: namely, geometric eigenmode decomposition of ultrahigh field-strength 7T fMRI. Crucially, this decomposition method investigates synchronous, distributed neural activity across the whole cerebral cortex—providing an enhanced understanding of large-scale dynamics that go beyond spatially localized signals. Compared to prior papers that have investigated the basic functional activity of the brain during ACAM-J, we aimed to characterize the extent of coupling between the brain's functional activity and its underlying structure by interrogating the contributions of global structural patterns at differing spatial scales, ranging from entire hemisphere to a few millimeters (Luppi et al. 2024).

Distributed cortical dynamics can be characterized by decomposing their signals into frequency-specific brain modes, or eigenmodes, via the previously proposed mathematical framework of eigenmode decomposition (Atasoy et al. 2016; Pang et al. 2023). Laplacian eigenmode decomposition can be used to decompose functional brain signals into elemental brain states at different spatial scales, which are thought to serve as building blocks of macro-scale neural activity (Atasoy et al. 2016; Atasoy et al. 2017; Atasoy et al. 2018a; Luppi et al. 2023), though the functional relevance of these eigenmodes is still unclear (Proix et al. 2023; Shinn 2023). This analysis framework represents brain activity (measured using blood oxygenation level dependent [BOLD] fMRI) as constrained by its underlying surface geometry and/or connectome structure—with eigenmodes describing the preferred patterns of vibration at the same frequency in a system of connected elements. Lower-numbered eigenmodes capture coarse-grained, large-scale spatial patterns with low spatial frequencies (e.g. separating left/right hemisphere, anterior/posterior regions, ventral/dorsal regions; see Fig. 1). In contrast, higher-numbered eigenmodes have higher spatial frequency and correspond to finer-grained, smaller-scale spatial patterns where functional properties of neighboring regions can vary independently of their spatial proximity. There have been two proposed approaches for neural Laplacian eigenmode decomposition: (i) connectome and (ii) geometric. While connectome eigenmodes, which have been called connectome harmonics, are derived from a structural connectome that estimates both local and long-range connections (derived using structural T1-weighted [T1w] and diffusion magnetic resonance MRI-based neuroimaging), geometric eigenmodes are derived from the cortical geometry of the brain and include just local connections (the shape of the cortex derived from structural T1w imaging). Broadly, the Laplacian eigenmode decomposition framework characterizes emerging spatiotemporal patterns in cortical functional dynamics as excitations of fundamental, resonant modes of the brain's structure (likened to how harmonics arise from the vibrations of a plucked violin string; Pang et al. 2023). Studies employing geometric and connectome eigenmodes decompositions have demonstrated successful, meaningful analysis decoding diverse conscious states: psychedelic-induced states (Atasoy et al. 2017; Atasoy et al. 2018b; Luppi et al. 2023), loss of consciousness (Luppi et al. 2023), vegetative/minimally conscious states (Luppi et al. 2023), task-evoked brain activity (Pang et al. 2023; Mansour et al. 2024; Vohryzek et al. 2024), and focused attention meditation (Atasoy et al. 2023). For example, recent studies have demonstrated connectome eigenmodes' ability to reconstruct spatial patterns of canonical functional networks (Atasoy et al. 2016; Preti and Van De Ville 2019). Connectome eigenmodes have also been expanded to the functional domain, showing that activity patterns elicited by seven different tasks are reconstructed from a small subset of functional harmonics (Glomb et al. 2021). Additionally, both geometric and connectome eigenmodes have consistently shown parsimonious, robust reconstruction accuracy of both empiric spontaneous and distinct task-evoked activation patterns (Pang et al. 2023; Mansour et al. 2024; Vohryzek et al. 2024). Crucially, geometric and connectome eigenmode decomposition, like the Fourier analysis, results in modes ordered by frequency, topological, and spatial, respectively, for geometric and connectome eigenmodes. This allows for multiscale investigation of the neural signatures of varying human conscious states using fundamental physical properties such as power of activation (magnitude of brain state activation) and energy (frequency-weighted power). Changes in consciousness induced

Downloaded from https://academic.oup.com/cercor/article/35/2/bhaf039/8046926 by Harvard Biostatistics user on 04 March 2025

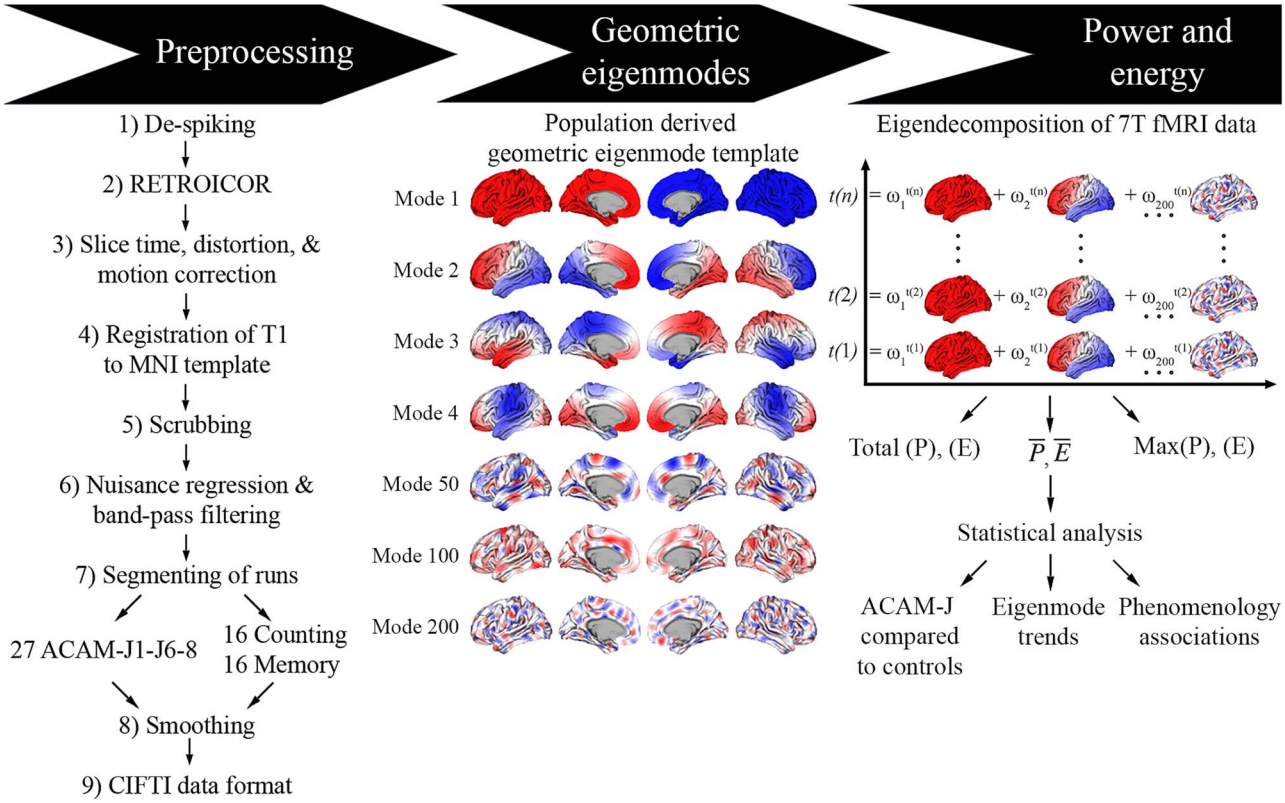

Fig. 1. Workflow of geometric eigenmode decomposition analysis. Raw 7 Tesla fMRI data were preprocessed and split into ACAM-J1 through ACAM-J6-8 segments for each of the 27 ACAM-J runs and 16 1-min segments for each of the non-meditative control tasks. Geometric eigenmode decomposition of the fMRI data was conducted using the population-derived geometric eigenmode template from Pang et al. (2023). The geometric eigenmodes were used to decompose fMRI brain activity data at a given time point [t(n)] as the sum of the modes weighted by their temporal activation in the fMRI data (ω for mode number k) at a given time point [ω_kt(n)]. Then, the total, mean ($\overline{P}$, $\overline{E}$), and maximum power and energy were calculated for each of the resulting eigenmode activation. Finally, statistical analyses were performed on the power and energy values, analyzing the ACAM-J compared to non-meditative controls, eigenmode polynomial trends, and associations with phenomenology ratings.

by psychedelics, anesthesia, severe brain injury, and stages of sleep all have been shown to be related to distinct alterations in the power and energy distribution of connectome eigenmodes (Atasoy et al. 2016; Atasoy et al. 2017; Rué-Queralt et al. 2021; Luppi et al. 2023). Relatedly, a preprint study found that focused attention meditation, compared to rest, was associated with increased global power, energy, and complexity of the brain activity as well as an expanded the repertoire of active brain states (Atasoy et al. 2023). Finally, a benefit of the geometric and connectome eigenmode decomposition approach is in linking the properties of these fundamental brain modes with subject phenomenological reports. For example, lysergic acid diethylamide (LSD) has been shown to induce energy changes in low-frequency connectome eigenmodes that are significantly correlated with emotional arousal and in the broader eigenmode frequency range that relate to ego dissolution and positive mood (Atasoy et al. 2017). Overall, resonance patterns captured by eigenmodes represent unique, distributed brain activation patterns in a manner that regional activity analyses fail to capture (Atasoy et al. 2016; Preti and Van De Ville 2019; Rué-Queralt et al. 2021; Pang et al. 2023). Thus, the connectome and geometric eigenmode decomposition framework serves as a valuable method to parse neural signatures of highly refined conscious states—such as ACAM-J—and link them meaningfully to subjective reports (Luppi et al. 2023).

For this study on ACAM-J, we used a geometric eigenmode decomposition analysis due to the scope of the study's objectives and available population-derived eigenmode templates, though future research may expand to include both connectome and geometric eigenmodes. The geometric eigenmode decomposition of ultrahigh field-strength 7T ACAM-J fMRI data, specifically, allows for the examination of the fundamental brain states that build into complex brain dynamics comprising subtle and refined conscious states. Additionally, this analysis framework provides a distinct lens with which to relate fundamental brain state properties of individual ACAM-J states with their rich phenomenological qualities (Sayadaw 2008; Sparby and Sacchet 2022; Sparby and Sacchet 2024; Yang et al. 2024a). In this context, the current study aimed to investigate three central questions: (i) What are the unique brain state power and energy patterns associated with ACAM-J cortical dynamics? (ii) How do brain state power and energy patterns during ACAM-J compare to non-meditative state cortical dynamics? (iii) How does meditative phenomenology relate to brain state activation during ACAM-J? To address these aims, we conducted a geometric eigenmode-based decomposition analysis of brain activity during ACAM-J and non-meditative control conditions using a high magnetic field-strength of 7 Tesla fMRI. We hypothesized that different ACAM-J states would exhibit shifts in underlying brain state power and energy dynamics compared to non-meditative control conditions similar to those observed in psychedelic states—that is, elevated global power and energy with a shift toward activation of higher frequency eigenmodes. We reasoned that the neurophysiological differences between ACAM-J and

Downloaded from https://academic.oup.com/cercor/article/35/2/bhaf039/8046926 by Harvard Biostatistics user on 04 March 2025

non-meditative tasks, or between LSD and placebo/resting-state, would demonstrate similar directionality in the changes to eigenmode power and energy given that both non-meditative and resting-state control conditions could be viewed as everyday cognitive states distinct from states induced by meditation or psychedelics, respectively. Additionally, we expected to see the eigenmode fMRI metrics indicating magnitude and range of brain state activation (total, mean and maximum power and energy) to exhibit correlations with subjective phenomenological reports related to attention, ACAM-J intensity, and sensations experienced during ACAM-J.

Materials and methods

This study used data from our intensive case-study design described at length previously (Yang et al. 2024a). Below, we provide an explanation of these methods and materials.

Case study participant

The subject was 52 years old at the time of the study. The participant was an experienced meditator and meditation instructor with more than 25 years of experience in ACAM-J. Based on an estimated daily practice of 1 h and around 1 year of retreat with 14 h of daily practice, their total estimated practice time amounted to 23,110 h. The participant practiced more of a sutta-style rather than the Visuddhimagga-style ACAM-J, as the participant reported using the breath, bodily feelings, and width of attention to enter ACAM-J. Prior to neuroimaging sessions, the participant was evaluated using the Mini-International Neuropsychiatric Interview (Sheehan et al. 1998) and Mini-Mental State Examination (Folstein et al. 1975), displaying no such neuropsychiatric or cognitive impairment diagnoses. The study received approval from the Mass General Brigham Institutional Review Board (IRB), and the participant provided informed consent.

Experimental design

ACAM-J

Briefly, fMRI data were gathered over five consecutive days, with each daily data collection session for ACAM-J lasting approximately 45 to 90 min, depending on the participant's fatigue and comfort levels. The participant followed their standard ACAM-J sequence with closed eyes, progressing from access concentration through ACAM-J1 to ACAM-J8, concluding with a post-ACAM-J8 state referred to as "afterglow." The participant marked transitions from access concentration to ACAM-J6 with a button press but did not indicate transitions from ACAM-J6 to ACAM-J7 nor from ACAM-J7 to ACAM-J8, as it would disrupt the natural flow of ACAM-J practice (this period is collectively reported as ACAM-J6-8 hereafter). In total, 27 runs of ACAM-J were recorded, and the average duration for a complete run covering ACAM-J1 to ACAM-J6-8 was 512.01 s (8.53 min; for more details on state duration, refer to Table S1). Importantly, studying ACAM-J using this methodology has demonstrated good within-subject reliability of fMRI brain responses associated with ACAM-J6-8 (Ganesan et al. 2024). The intensive case-study design allows for acquisition of high-quality data from an advanced, rare practitioner yet with the power of repeated measurement. In the initial investigation of advanced meditative phenomenon, the intensive case-study paradigm is a powerful tool in avoiding potential masking of idiosyncratic, subject-specific effects while allowing for corroboration of specific effects in later group sample studies as demonstrated by (Trautwein et al. 2024) building on prior single case study by (Dor-Ziderman et al. 2016).

Non-meditative control states

Two non-meditative control conditions were developed for comparison with meditation states, aimed at engaging the participant's mind in non-meditative, everyday cognitions while avoiding the induction of meditative states. Resting-state control was not used due to concerns that experienced meditators might enter meditative states during rest, which may complicate interpretations of results (Tang et al. 2012). We elected not to use a basic mindfulness condition as a control given that at the meditation experience level of the practitioner studied, it would be difficult for them to practice pure mindfulness without inadvertently transitioning into ACAM-J or other forms of advanced meditation with sometimes rich and complex phenomenology. These control conditions consider the phenomenology of meditative states and the nature of the experimental paradigm to ensure greater consistency and reliability in the intensive case-study design (Yang et al. 2024a). The two control conditions involved a memory task, where the participant recalled events from the past 2 weeks, and a counting task, where the participant mentally counted down from 10,000 in decrements of 5. Two 8-min runs of each non-meditative control were collected (totaling 16 min of data for each condition). Although the case study participant reported experiencing a small degree of ACAM-J during the first 8 min of the control conditions, these meditative qualities were not nearly as intense as the volitional meditation states experienced during their meditation runs, and this did not impact the differences between ACAM-J and non-meditative controls in prior analyses (Yang et al. 2024a). A supplementary analysis was conducted excluding the first 8 min of each control condition, and the results are reported in Supplementary Results Figs. S1–S3 and Supplementary Data 2.

Phenomenology

To complement objective neuroimaging data, this study design also used a first-person phenomenological approach, in which the subject assessed the mental and physiological processes relevant to the experience of ACAM-J as they manifested during meditation (using a prior described approach; Yang et al. 2024a). In brief, following a complete ACAM-J run (ACAM-J1 to ACAM-J8), the participant assigned a rating from 1 to 10 for phenomenological items including: (i) "stability of attention," ranging from poor to excellent stability; (ii) "width of attention," varying from a narrow scope like a laser to very wide like a fisheye lens; (iii) "intensity of ACAM-J," indicating how intense a specific ACAM-J quality was; (iv) "early phenomenology of sights, sounds, physical sensations, and narrative thought stream," denoted by the presence of sights, sounds, physical sensations, and narrative thought contents during the form ACAM-J (ACAM-J1-J4); and (v) "late phenomenology of sights, sounds, physical sensations, and narrative thought stream," characterized by the presence of sights, sounds, physical sensations, and narrative thought contents during the formless ACAM-J (ACAM-J5 and ACAM-J6-8). Higher rating values indicated a more robust experience within the given item. "Stability of attention, width of attention, and intensity of ACAM-J" were rated for each ACAM-J in each run (27 runs with ratings for each of the 6 states: ACAM-J1-J6-8). Phenomenology of "sights, sounds, physical sensations, and narrative thought stream" was rated separately for early (ACAM-J1 to J4) and late (ACAM-J5 and ACAM-J6-8) aggregate states for each run (27 runs with 2 ratings for early and late ACAM-J states).

Downloaded from https://academic.oup.com/cercor/article/35/2/bhaf039/8046926 by Harvard Biostatistics user on 04 March 2025

Neuroimaging acquisition

Neuroimaging scans were obtained utilizing a 7T magnetic resonance (MR) scanner (SIEMENS MAGNETOM Terra) equipped with a 32-channel head coil. Functional imaging utilized a single-shot two-dimensional echo planar imaging sequence with T2∗-weighted BOLD-sensitive MRI. The imaging parameters included a repetition time (TR) of 2.9 s, an echo time (TE) of 30 ms, a flip angle (FA) of 75°, a field of view (FOV) of [189 × 255], a matrix of [172 × 232], GRAPPA factor of 3, a voxel size of $1.1 \times 1.1 \times 1.1$ mm^3, 126 slices, an interslice distance of 0 mm, bandwidth of 1540 Hz/px, and an echo spacing of 0.75 ms. Slice acquisitions covered the entire brain, with interleaved slices, sagittal orientation, and anterior-to-posterior phase encoding. Additionally, opposite phase-encoded slices (i.e. posterior to anterior) with identical parameters were acquired for distortion correction.

Whole-brain T1-weighted structural images were acquired with the following parameters: a TR of 2.53 s, a TE of 1.65 ms, an inversion time of 1.1 s, a flip angle of 7°, 0.8 mm isotropic resolution, an FOV of 240 × 240, a GRAPPA factor of 2, and a bandwidth of 1200 Hz/Px. Physiological signals, including heart rate (measured using pulse oximetry) and respiration (recorded with breathing bellows), were continuously monitored throughout the scanning session.

Neuroimaging preprocessing

In brief, preprocessing pipeline encompassed the following steps: (i) de-spiking, (ii) RETROspective Image CORrection (RETROICOR)), (iii) slice time correction, (iv) distortion correction, (v) motion correction, (vi) registration of the anatomical dataset (T1w) to a standard MNI template, (vii) scrubbing and removal of any volume with motion >0.3 mm and more than 5% outlier voxels, (viii) regression of eroded cerebrospinal fluid mask time course and motion parameters (3 translations, 3 rotations) per run, and finally band-pass filtering (0.01 to 0.1 Hz; Cox 1996). Each fMRI run was then partitioned into distinct segments corresponding to different ACAM-J conditions (27 segments for each ACAM-J state). Moreover, each control run was further divided into 1-min segments to ensure comparability with the 2-min segments of each ACAM-J. This resulted in a total of 16 segments for each control condition, providing a robust basis for statistical comparisons with the ACAM-J. Due to comparable duration, we call the partitioned fMRI data of both control and ACAM-J runs "segments" for the purpose of analysis. Finally, (ix) the bias field of the T1 image was corrected using SPM12 (Friston 2011), all fMRI data were smoothed with surface smoothing of 6 mm full width at half maximum (FWHM) and was converted to CIFTI data format for further processing using ciftify_recon_all and ciftify_subject_fmri (Glasser et al. 2013).

Geometric eigenmode decomposition

In order to decompose fMRI activity into 200 frequency-specific eigenmodes (Fig. 1), we used geometric eigenmodes derived from a population-averaged midsurface thickness template of the neocortical surface from Pang et al. (2023), wherein the methods to generate these geometric eigenmode templates are also described. We used template geometric eigenmodes for this analysis (i) to ensure standardization of a population-derived atlas given the single participant design of the study and, (ii) as previous work has shown, geometric eigenmode decomposition results were not affected by use of population-derived eigenmode templates compared to subject-specific surface derived eigenmodes (Pang et al. 2023). Briefly, the geometric eigenmodes were computed by applying the Laplace–Beltrami operator (LBO) onto the cortical mesh and estimating its eigenvectors by solving the eigenvalue problem. The resulting eigenvalues relate to spatial frequency/wavelength of each mode, where mode 1 has the longest spatial wavelength (lowest spatial frequency) while higher modes have shorter wavelengths (higher frequency). Conversely, the geometric eigenmodes yield an orthogonal function basis—ie any spatial pattern on the cortex can be represented as a weighted sum of the geometric eigenmodes.

Using the geometric eigenmodes, we decomposed functional MRI data to reveal emerging cortical spatiotemporal dynamic patterns by examining the contribution of each eigenmode to the cortical activity at each time instance. At each time point of the non-meditative control and ACAM-J fMRI time courses, the fMRI data were projected onto each of the 200 geometric eigenmodes, yielding the temporal activity of the particular eigenmode in a method described previously (Atasoy et al. 2016; Atasoy et al. 2017). Subsequently, the temporal activation of eigenmodes were analyzed in terms of their power and energy at each fMRI time point. Here, power is defined as the strength of an eigenmode's activation at a given fMRI time instance: $|\omega_k(t_i)|$. Alternatively, energy is the eigenmode's frequency-weighted contribution, estimated by weighting the square of the eigenmode's strength of activation by the square of its corresponding eigenvalue (i.e. its intrinsic energy [λ_k]) at each time point: $|\omega_k(t_i)|^2\ \lambda_k{}^2$. Mean power and energy were calculated by averaging the power and energy of each eigenmode across all time points in a single ACAM-J or non-meditative control fMRI segment (i.e. yielding mean power and energy values for each of the 200 modes per fMRI segment). Maximum power and energy were calculated as the maximum spectra value for a given eigenmode across all time points within a segment (i.e. yielding 200 maximum power and energy values for 200 modes per fMRI segment). Unless otherwise noted, all reported maximum and mean power and energy values are reported on a log scale (Atasoy et al. 2017). Brain total power and total energy were computed by summing power and energy across all eigenmodes for each time point and then averaging all time points within a segment.

Statistical analysis

Global power and energy patterns across ACAM-J and control conditions

All statistical analyses and visualizations were conducted in Python unless otherwise noted. To analyze global cortical dynamic patterns across ACAM-J and control conditions, we conducted a linear mixed model analysis in R using the *lme4* and *lmeTest* packages (Bates et al. 2015; Kuznetsova et al. 2017; R-Core-Team 2023) comparing the mean power and energy values of each ACAM-J to each of the control conditions as the reference group separately (memory, counting). Segments were set as random intercept components with condition (ACAM-J1 to J6-8, control condition) and eigenmodes (log) as fixed effects, and an additional interaction term between the conditions and eigenmode (log) value. Using this approach, linear model estimates for each of the ACAM-J states compared to the control conditions represented global total and mean power and energy patterns (non-frequency specific), while slope differences were used to parse differences in frequency-specific mean power and energy over the 200 eigenmodes. Likewise, to assess brain total power and total energy patterns, we conducted additional linear mixed models comparing all ACAM-J to each control condition using total power and energy values. Segments were again set

Downloaded from https://academic.oup.com/cercor/article/35/2/bhaf039/8046926 by Harvard Biostatistics user on 04 March 2025

as random intercept components with condition as the fixed effect. All *P*-values were corrected using the false discovery rate (FDR) using the Benjamini–Hochberg approach across all model parameters (Benjamini and Hochberg 1995). Additionally, Kolmogorov–Smirnov tests were conducted to assess differences in the total power and energy distributions between each control condition and the different ACAM-J states. The *P*-values were FDR-corrected across each control comparison.

Eigenmode power and energy across ACAM-J and control conditions

To further analyze differences in frequency-specific eigenmode mean power and energy across the ACAM-J and control conditions while minimizing multiple comparisons, we used 15 eigengroups (groups 0 to 14), grouping eigenmodes according to spatial frequency as calculated based on a sphere radius ≈67 mm by the equation:

$$\text{wavelength} = \frac{2\pi R_s}{\sqrt{l\,(l+1)}},$$

(Chen et al. 2022; Pang et al. 2023), where R_s is the radius of the sphere and l is the eigengroup. Eigengroups provide a way to aggregate degenerate solutions from the solving of the eigendecomposition of the LBO (see *Geometric eigenmode decomposition*) such that eigenmodes with the same number of nodal lines and wavelengths are grouped together. As such, low numbered eigengroups correspond to large-scale spatial patterns while high numbered eigengroups correspond to finer-grained spatial patterns. This method allows for investigation of eigenmode metrics that are less affected by noise (Boyes et al. 2024; Cao et al. 2024). Using this approach, each eigengroup's power and energy were then compared as reference values to both counting and memory control conditions using a Dunnett's test. The resulting *p*-values were FDR corrected across both control condition comparisons within a single ACAM-J state. This resulted in 180 comparisons (15 eigengroups, 2 controls for 6 different ACAM-J periods).

Eigenmode power and energy trends within ACAM-J

Given the sequential trajectory of ACAM-J, we aimed to investigate power and energy trends across this progression by fitting polynomial models for each eigenmode across the 6 ACAM-J. Thus, we tested the cubic, quadratic, and linear model fit of each eigenmode's mean power and energy values from ACAM-J1 to ACAM-J6-8. The models were fit up to a third-order polynomial to elucidate linear and nonlinear patterns in brain activity (Galante et al. 2023) as the participant moves through ACAM-J while preventing overfitting (Yang et al. 2024a). To do this, the ACAM-J condition was centered; then, the centered linear terms were both cubed and squared to compute the corresponding cubic and quadratic ACAM-J condition terms. Next, a linear mixed model was implemented with each run as a random intercept component and ACAM-J as a fixed effect with a third-order polynomial slope (i.e. cubic, quadratic, and linear terms included) for mean power or the mean energy predictor variable. If the highest-order term's slope was not statistically significant or the model exhibited singularity, the highest-order term was iteratively eliminated, and the model was re-evaluated. This process continued until either the highest term reached significance or only the linear term persisted and was repeated for each of the 200 eigenmodes in order to construct a simpler yet interpretable model for each of the brain states. This resulted in the highest-order significant (or nonsignificant linear) polynomial model for each eigenmode's mean power and energy data across the ACAM-J1 to ACAM-J6-8 trajectory. The *P*-values of all final model terms were FDR-corrected within each group of parameter terms (e.g. across cubic term *P*-values, across quadratic term *P*-values, across linear term *P*-values).

Phenomenological analysis across ACAM-J

To relate underlying brain state properties during ACAM-J to their phenomenological qualities, we used both Pearson correlation and ordinary least squares (OLS) linear regression models (Seabold and Perktold 2010). Phenomenology items included were (i) "stability of attention," (ii) "width of attention," (iii) "intensity of ACAM-J," (iv) "early (ACAM-J1-J4) phenomenology of sights, sounds, physical sensations, and narrative thought stream" (collectively referred to as "early phenomenology") and (v) "late (ACAM-J5 and ACAM-J6-8 phenomenology of sights, sounds, physical sensations, and narrative thought stream" (collectively referred to as "late phenomenology"). These ratings were correlated with global total, mean, and maximum power and energy values using Pearson correlation. For these global phenomenological analyses, spectra values were averaged across the 200 eigenmodes and all six ACAM-J states when correlated with ratings of "stability of attention," "width of attention," and "intensity of ACAM-J" across ACAM-J1-J6-8. ACAM-J1-J4 spectral data were included for early phenomenology global correlations, and only ACAM-J5 and ACAM-J6-8 spectral data were included for late phenomenology global correlations. To assess frequency-specific associations, phenomenological items were also correlated with eigengroup maximum and mean power and energy spectrum data using Pearson correlations for ratings of stability of attention, width of attention, and intensity of ACAM-J (rated for each state). For ratings of early phenomenology and late phenomenology, which were rated for an aggregate group of states, we used a multiple linear regression to assess both eigengroup maximum and mean power and energy data. This was done in order to parse individual ACAM-J state's contribution to the relationship between maximum and mean eigenmode spectra values and the aggregate ratings of early or late phenomenology. All resulting *P*-values values were FDR-corrected to reduce false-positive rates.

Results

Global power and energy patterns across ACAM-J and control conditions

Linear mixed model results revealed that, globally, ACAM-J2, ACAM-J3, and ACAM-J6-J8 had significantly higher mean power compared to both counting and memory control conditions (Figs. 2A and B and 3A and B). In contrast, ACAM-J5 had significantly higher global mean power compared to the memory control condition only. No global significant mean energy differences were observed across any conditions (Supplementary Data 1).

Analyses on total power and total energy indicated that specific ACAM-J states show altered total power and total energy value distributions (summed over all eigenmodes) compared to both control conditions. Notably, during ACAM-J2, ACAM-J3, and ACAM-J6-J8, the total power and energy distributions differed significantly from the counting and memory conditions (Fig. 2C and D). Additionally, ACAM-J5 had different total power distributions compared to the counting control condition and differing energy distribution compared to the memory control condition only, while ACAM-J1 and ACAM-J4 had different total power distributions

Downloaded from https://academic.oup.com/cercor/article/35/2/bhaf039/8046926 by Harvard Biostatistics user on 04 March 2025

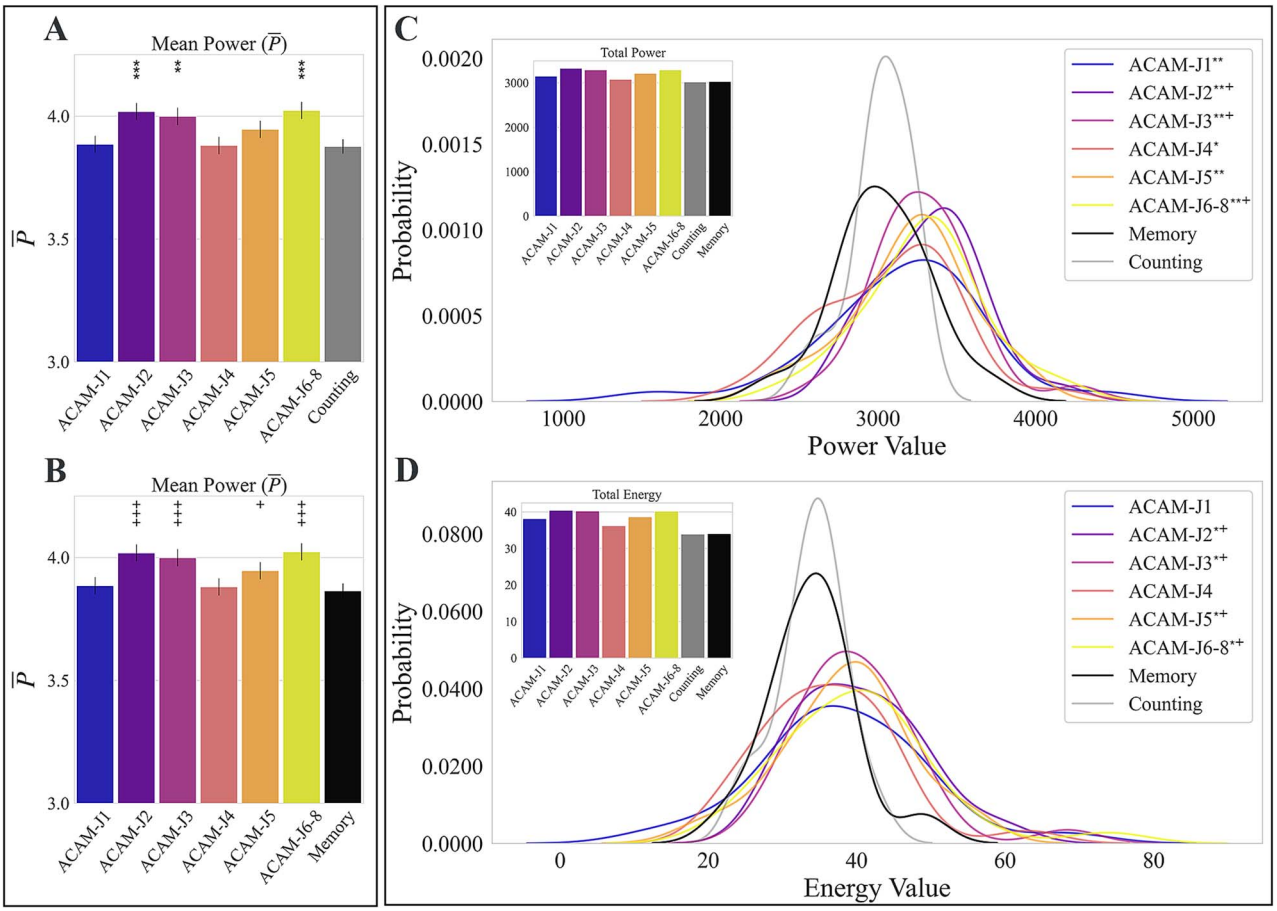

Fig. 2. Global eigenmode mean power and total energy values for ACAM-J and non-meditative control tasks. The left panel visualizes linear mixed model estimate values for logged mean power ($\overline{P}$) averaged across all 200 eigenmodes for ACAM-J1-J6-8 compared to the A) counting and B) memory task. In the right panel, the bar chart depicts the total C) power and D) energy values in all ACAM-J and both non-meditative control tasks (sum over all eigenmodes), while the line graph maps the significance of probability distribution of C) power and D) energy states using the Kolmogorov Smirnov test. $^{*}P_{\text{FDR-counting}} < 0.05$, $^{**}P_{\text{FDR-counting}} < 0.01$, $^{***}P_{\text{FDR-counting}} < 0.001$. $^{+}P_{\text{FDR-memory}} < 0.05$, $^{++}P_{\text{FDR-memory}} < 0.01$, $^{+++}P_{\text{FDR-memory}} < 0.001$.

compared to the counting control. As visualized in Fig. 2C and D, the control conditions had a lower peak value on the power and energy spectrum compared to most ACAM-J. The power and energy distributions of both counting and memory conditions were also less widely distributed compared those of ACAM-J. Encouragingly, no significant differences were observed between the two non-meditative control condition distributions themselves in either total energy or total power ($P > 0.05$). Unlike distributions, differences in the global total power and energy levels of ACAM-J and control conditions were not significant after FDR correction.

Frequency-specific brain state power and energy across ACAM-J and control conditions

Mean power of ACAM-J6-8 had a steeper slope compared to the memory condition ($b = -0.304$, $P_{\text{FDR}} = 0.035$), indicating a sharper decrease in mean power across the eigenmodes compared to the memory condition (Fig. 3B). No other slopes were significantly different from either control conditions.

Dunnett's tests of eigengroup mean power and energy signaled that eigenmode mean power and energy were significantly higher than controls at specific eigengroups in ACAM-J2, ACAM-J3, and ACAM-J6-J8 (Fig. 4). ACAM-J2 had higher mean power compared to both control conditions in 7 out of 15 eigengroups (eigengroups 1 to 2, 4, 7 to 9, and 11). Additionally, ACAM-J2 had higher mean power than the counting control condition in eigengroups 0 and 14 and had higher mean energy than the memory control condition in eigengroups 3, 6, and 12. ACAM-J3 had higher mean power compared to both control conditions in 4 out of 15 eigengroups (eigengroups 1 and 9 to 11) as well as higher mean power than the counting control condition in eigengroups 0, 4, and 7 to 11 and higher mean power than the memory control condition in eigengroups 2 and 6. ACAM-J6-8 had higher mean power compared to both control conditions in 4 out of 15 eigengroups (eigengroups 1, 3, and 8 to 9) as well as higher mean power than the counting control condition in eigengroups 4 and 7 and higher mean power than the memory control condition in eigengroups 2 and 6.

Moreover, mean energy analyses revealed ACAM-J2 had higher mean energy compared to both control conditions in 11 out of 15 eigengroups (eigengroups 1 to 2, 4, 6 to 12, and 14). ACAM-J2 also had higher mean energy than the counting control condition in eigengroups 0 and 13 and higher than the memory control condition in eigengroup 3. ACAM-J3 had higher mean energy compared to both control conditions in 8 out of 15 eigengroups (eigengroups 1, 4, and 7 to 12). Additionally, ACAM-J3 had higher mean energy than the counting control condition in eigengroup 0 and higher than the memory control condition in eigengroups 2 and 6. Finally, ACAM-J6-8 had higher mean energy compared to both control conditions in 10 out of 15 eigengroups (eigengroups 1, 3 to 4, and 6 to 12). ACAM-J6-8 also had higher mean energy compared to the counting control condition in eigengroup 14 and higher than the memory control condition in eigengroup 2.

Downloaded from https://academic.oup.com/cercor/article/35/2/bhaf039/8046926 by Harvard Biostatistics user on 04 March 2025

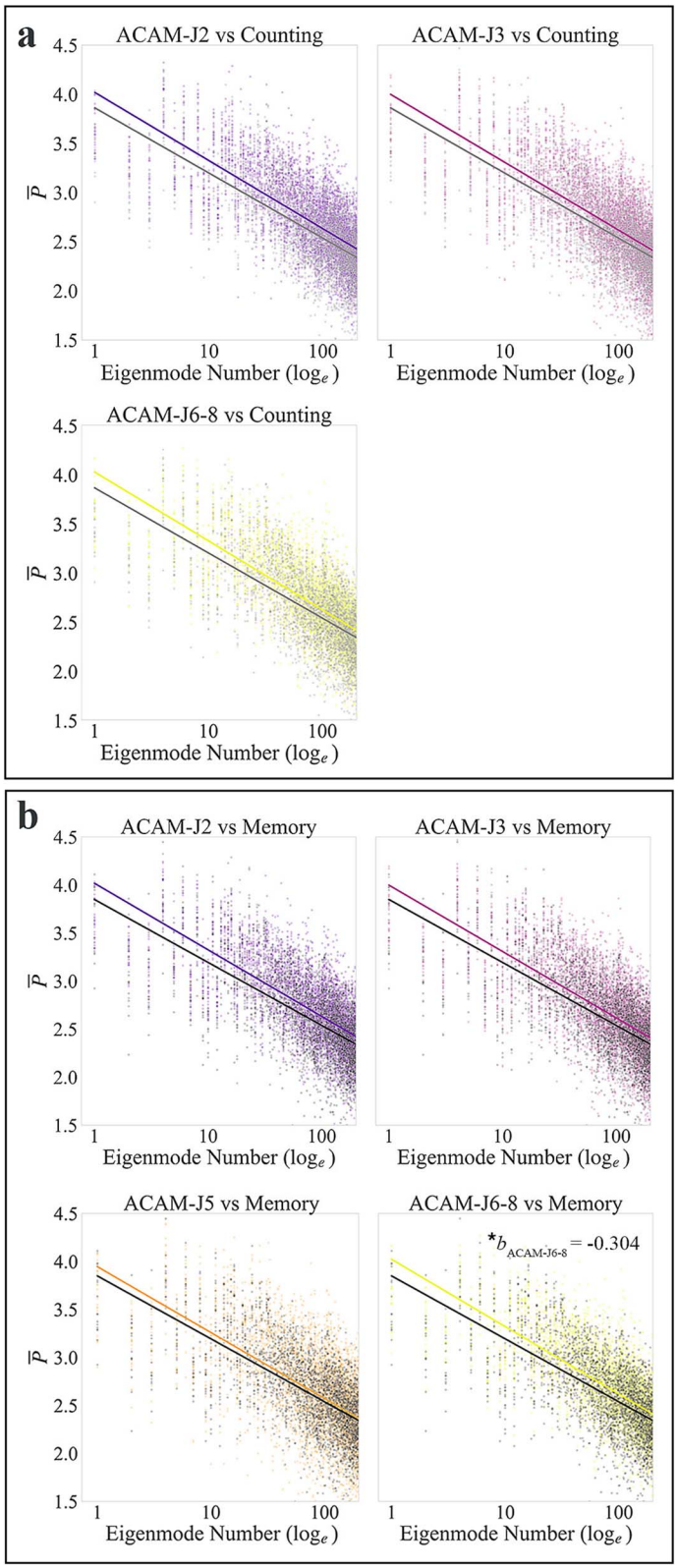

Fig. 3. Eigenmode mean power spectrum for ACAM-J compared to non-meditative control tasks. Logged mean power ($\overline{P}$) vs. eigenmode number ($\log_e$) spectra and best fit line for ACAM-J with significant ($P_{FDR} < 0.05$) global mean power differences compared to A) counting and B) memory task. Slope (b) values are reported for slopes that differed significantly ($P_{FDR} < 0.05$) between a control task and ACAM-J. *$P_{FDR} < 0.05$, **$P_{FDR} < 0.01$, ***$P_{FDR} < 0.001$.

Downloaded from https://academic.oup.com/cercor/article/35/2/bhaf039/8046926 by Harvard Biostatistics user on 04 March 2025

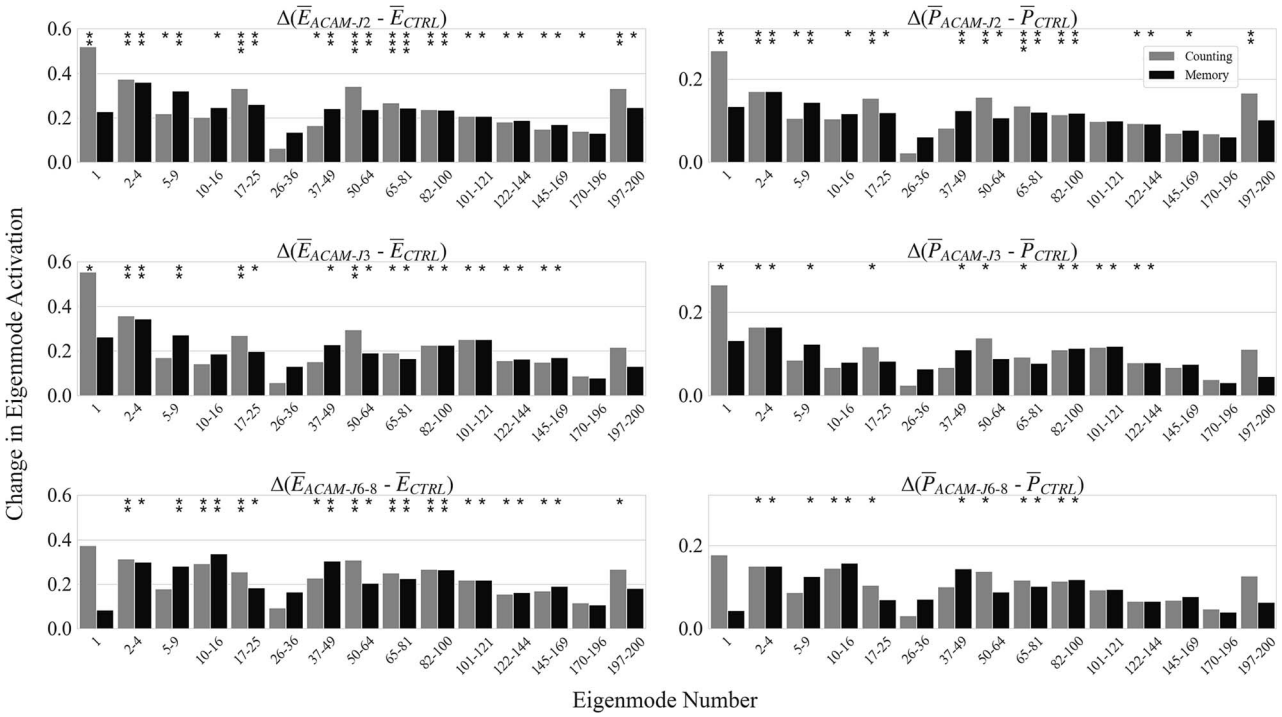

Fig. 4. Frequency-specific energy and power differences between ACAM-J and non-meditative control tasks. Mean energy ($\bar{E}$;left) and power ($\bar{P}$; right) differences of 15 eigengroups of ACAM-J2, ACAM-J3, and ACAM-J6-8 compared to memory (black) and counting (gray) tasks using Dunnett's test. ACAM-J1 and ACAM-J4 did not demonstrate any significant differences in eigengroup mean power or energy. Eigenmodes in each eigengroup are detailed on the *x* axis of each plot, with lower number eigenmodes corresponding to large-scale spatial patterns and higher number eigenmodes corresponding to finer-grained spatial patterns. $^{*}P_{FDR} < 0.05$, $^{**}P_{FDR} < 0.01$, $^{***}P_{FDR} < 0.001$.

Eigenmode power and energy model trends across ACAM-J

Polynomial model trends of eigenmode mean power and energy across the progression from ACAM-J1-J6-8 demonstrated robust positive cubic trends (Fig. 5A and D). Eigenmode mean power analysis yielded 56 significant eigenmode cubic trends (28%) and 2 significant eigenmode linear trends (1%), all with positive coefficient terms (Fig. 5A). Similarly, mean energy analysis yielded 62 significant eigenmode cubic trends (31%) and 2 significant eigenmode linear trends (1%), all with positive coefficient terms (Fig. 5D). Positive cubic curves represent an increase of spectra values to peak (local maximum), decrease to trough (local minimum), and subsequent increase again across ACAM-J6-8 within a given eigenmode. Specifically, these curves increase from ACAM-J1 to ACAM-J2, dip in ACAM-J5, and increase again in ACAM-J6-8 for both mean power and energy as illustrated by the black curves that depict the mean cubic trajectories in Fig. 5C and F. Notably, the magnitude of eigenmode mean energy cubic term coefficients were smaller compared to those of eigenmode mean power, indicating a less pronounced curve. For full significant model term polarity trends, see Table S1. A 10-bin histogram with kernel density estimate using Gaussian kernels demonstrates that most significant cubic eigenmodes were clustered around the middle of the eigenmode spectrum, in the 50 to 100 mode number range, for both power and energy (Fig. 5B and E).

Phenomenological analysis across ACAM-J

Global measures of total, mean, and maximum power and energy (averaged over ACAM-J and eigenmodes) all exhibited moderately strong positive correlations with ratings of "width of attention" (Fig. 6A). Ratings of "stability of attention" and "intensity of ACAM-J" also showed a significant correlation with global maximum power and maximum energy values. Global maximum power and energy values were positively correlated with "early phenomenology (ACAM-J1-J4) of sights," while they were negatively correlated with ratings of "early phenomenology of sounds." "Late phenomenology of sounds" (ACAM-J5 and ACAM-J6-8) exhibited a moderately strong negative correlation with total power and mean power values (Fig. 6B).

Ratings of "early phenomenology" also demonstrated frequency-specific associations with eigengroup maximum power and energy in ACAM-J1, ACAM-J2, and ACAM-J3 as well as eigengroup mean power and energy in ACAM-J2 and ACAM-J3. In ACAM-J1, a linear regression model of ratings of "early phenomenology" with eigengroup power and energy values revealed significant negative associations with "early phenomenology of sounds" in 6 out of 15 groups (eigengroups 1, 5, 8, 10, 11, and 14) for both maximum power and energy (Fig. 6C). In ACAM-J2 and ACAM-J3, ratings of "early phenomenology of sights" were positively associated with eigengroup maximum power and energy in eigengroup 1 (Fig. 6D and E). In ACAM-J2, eigengroup mean power was positively associated with "early phenomenology of sights" for 6 out of 15 groups (eigengroups 1, 3, 6, and 9 to 11), and eigengroup mean energy was positively associated with 2 additional eigengroups (eigengroups 8 and 13; Fig. 6F). In ACAM-J3, eigengroup mean power and mean energy were positively associated with "early phenomenology of sights" in 2 out of 10 groups (eigengroups 10 and 14), and eigengroup mean energy was positively associated with an additional group (eigengroup 9; Fig. 6G). No frequency-specific significant correlations were found between eigengroup mean power or energy and ratings of "stability of attention," "width of attention," "intensity of ACAM-J," and "late phenomenology" (Supplementary Data 1).

Downloaded from https://academic.oup.com/cercor/article/35/2/bhaf039/8046926 by Harvard Biostatistics user on 04 March 2025

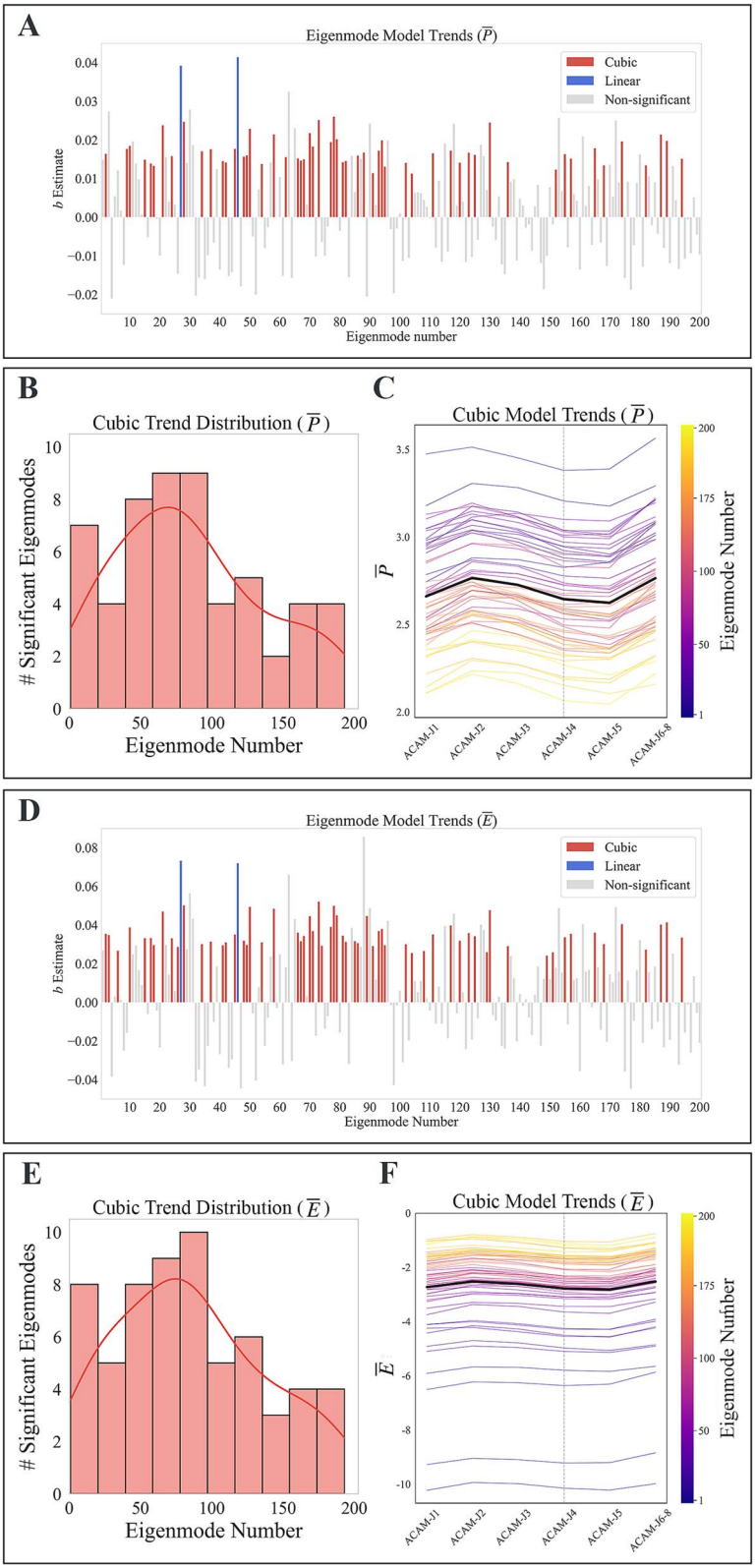

Fig. 5. Eigenmode power and energy model trends. Bar charts visualize parameter coefficient estimates (*b*) of the highest order or nonsignificant linear polynomial model for each eigenmode mean A) power and D) energy. Colored bars indicate $P_{FDR} < 0.05$ for the highest-order model parameter. Histograms visualize distribution of significant cubic model eigenmodes with a kernel density estimate for mean B) power and E) energy. Line graphs show best fit cubic models for significant cubic eigenmode mean C) power and F) energy, with color corresponding to eigenmode number. Black curve reflects the average cubic eigenmode trend, and dashed vertical line represents transition from form ACAM-*J* to formless ACAM-*J*.

Downloaded from https://academic.oup.com/cercor/article/35/2/bhaf039/8046926 by Harvard Biostatistics user on 04 March 2025

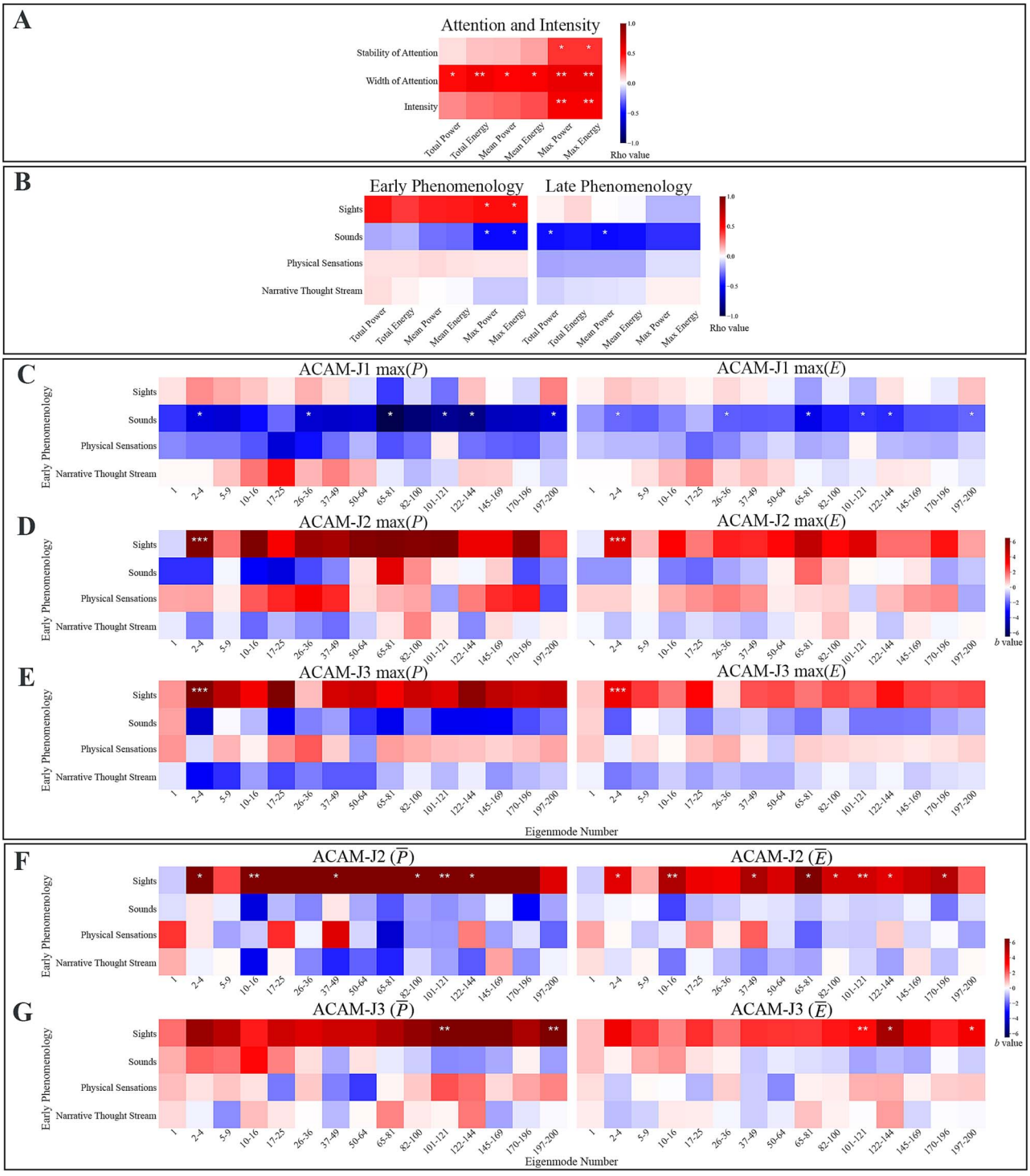

Fig. 6. Associations between phenomenology ratings and eigenmode power and energy. A) Pearson correlation between global eigenmode total, mean, and maximum power and energy values and ratings of "stability of attention, width of attention, and intensity of ACAM-J." B) Pearson correlation between global eigenmode total, mean, and maximum power and energy values and ratings of "early phenomenology" (ACAM-J1 to J4) and "late phenomenology" (ACAM-J5 and ACAM-J6-8) of "sights, sounds, physical sensations, and narrative thought stream" with FDR correction. Linear regression coefficient values (*b*) of frequency-specific associations between "early phenomenology of sights, sounds, physical sensations, and narrative thought stream" and 15 eigengroup C) maximum power and energy during ACAM-J1, D) mean power and energy during ACAM-J1, E) mean power and energy during ACAM-J2, and F) mean power and energy during ACAM-J3 with FDR correction and Bonferroni correction of linear regression terms. Eigenmodes in each eigengroup are detailed on the x axis of each plot. $^{*}P_{FDR} < 0.05$, $^{**}P_{FDR} < 0.01$, $^{***}P_{FDR} < 0.001$.

Supplemental control analyses

Results of the supplementary analyses using only segments 9 to 16 of the non-meditative control conditions are reported in Supplementary Results Figs. S1–S3 and Supplementary Data 2. Results supported the patterns described above with minimal differences from analyses using all control segments. In general, the results observed were strengthened when control segments 1 to 8 were excluded, with ACAM-J5 additionally demonstrating

Downloaded from https://academic.oup.com/cercor/article/35/2/bhaf039/8046926 by Harvard Biostatistics user on 04 March 2025

increased mean power compared to both memory and control conditions and ACAM-J2, ACAM-J3, and ACAM-J6-8 showing elevated total power compared to the counting control condition. Additionally, ACAM-J2, ACAM-J3, and ACAM-J5 states demonstrated significantly steeper mean power slopes across 200 eigenmodes compared to the memory control condition, as observed in the results reported for ACAM-J6-8 in Fig. 3B. Dunnett's tests comparing eigengroup mean power and energy differences demonstrated some deviations in eigengroup significance compared to counting and memory control conditions, which are summarized in Supplementary Table S3. Eigengroup significant differences remained in ACAM-J2, ACAM-J3, and ACAM-J6-8 as in the main analyses. In general, more deviations were observed in eigengroup mean energy results compared to mean power, with fewer eigengroups demonstrating significant differences between ACAM-J and control conditions, particularly in ACAM-J6-8.

Discussion

This study implemented a geometric eigenmode decomposition of intensive case study ultrahigh field-strength 7T fMRI data to elucidate the fundamental brain states comprising the complex cortical dynamics associated with ACAM-J. Principal findings from the current investigation of advanced concentrative absorption meditative states include the following: (i) Select ACAM-J show elevated brain state power and energy patterns between ACAM-J states and compared to non-meditative control conditions, and (ii) specific ACAM-J phenomenological qualities were associated with both global and frequency-specific power and energy levels. These results point to the nonlinear pattern of brain state activation during the ACAM-J progression—providing valuable insight into the power and energy patterns characterizing these specific ACAM-J states and how those map meaningfully to phenomenological reports of attention, intensity, and sensations by the meditator. Crucially, brain modes demonstrate globally elevated power associated with reports of more stable, diffuse attention and intense ACAM-J quality in general (Fig. 6A).

Geometric eigenmode decomposition allows for the characterization of the distributed, elemental brain state activation (Atasoy et al. 2018a) during highly refined concentrative conscious states. Laplacian eigenmode decomposition approaches differ from traditional network or ROI-based neuroimaging analyses of ACAM-J, which only consider spatially localized or functional signals, respectively. Instead, Laplacian eigenmode decomposition offers an approach to examining brain activity that accounts for the interdependence of function and structure. This approach, along with other recent neuroimaging decomposition approaches, allows for the characterization of the context of functional interactions in the brain in terms of their temporal dynamics, distributed spatial scales, and type of information conveyed (Luppi et al. 2024). Geometric eigenmode decomposition falls within the distributed spatial scales portion of these investigations. Analyses from the growing literature of connectome and geometric eigenmode decomposition are complementary to ROI-based approaches and have successfully decoded various states of consciousness (Atasoy et al. 2016; Atasoy et al. 2017; Atasoy et al. 2018b; Preti and Van De Ville 2019; Glomb et al. 2021; Rué-Queralt et al. 2021; Atasoy et al. 2023; Luppi et al. 2023; Pang et al. 2023; Mansour et al. 2024; Vohryzek et al. 2024). Applying neuroimaging decomposition approaches such as geometric eigenmode decomposition to advanced meditation research holds promise for revealing insights into the natural global brain patterns that serve as building blocks of the neural activity associated with these practices.

Elevated brain state activation was observed most consistently during a subset of these states: ACAM-J2, ACAM-J3, and ACAM-J6-8 and occasionally ACAM-J5. These states exhibited differences in global mean power as well as total power and energy distributions from non-meditative control conditions (Fig. 2A–D). The increased global mean power of eigenmodes during ACAM-J2, ACAM-J3, ACAM-J5, and ACAM-J6-8 suggests overall stronger brain state activation (i.e. mean contribution to cortical dynamics) compared to non-meditative conditions—regardless of the coarseness of the eigenmode's spatial scale (i.e. frequency)—as the meditator builds on the meditative progression through the form and formless ACAM-J (Galante et al. 2023; Yang et al. 2024a). It is possible that the no significant differences observed in global mean energy between the ACAM-J and control conditions may be due to increased variance in the eigenmodes' frequency-weighted magnitude of contribution to the cortical dynamics (energy) compared to just their magnitude of contribution (power). Notably, no significant differences in global total (i.e. summed across 200 eigenmodes) power and energy levels between any of the ACAM-J conditions and controls were observed, which differs from elevated global power and energy observed in states induced by psychedelics (Atasoy et al. 2017; Luppi et al. 2023). This suggests that the disparity in brain state activation between ACAM-J and non-meditative states is more related to mean and varying probability distributions of power and energy levels. Crucially, the peaks of these total spectra distributions were shifted toward higher frequencies on the power and energy spectrums, meaning that there was a greater probability of obtaining higher total brain power and energy values during these periods compared to controls. The greater probability of achieving high energy states may reflect an expanded repertoire of brain state activation during these diverse conditions of consciousness (Luppi et al. 2023). Additionally, ACAM-J conditions' probability distributions appeared to have a wider spread across the power spectrum, which may indicate more diffuse power and energy values for these states compared to controls (Fig. 2C and D). These results complement and are consistent with a preprint connectome eigenmode-based decomposition analysis of a group of meditators engaged in focused attention meditation that found evidence for increased global power, energy, and complexity of the brain activity and an expanded the repertoire of active brain states during this meditation compared to resting state (Atasoy et al. 2023).

Furthermore, brain state globally elevated total, mean, and maximum power and energy were positively correlated with ratings of "width of attention" (Fig. 6A), suggesting that as the meditator enters absorptive meditation states characterized by greater and more dynamic power and energy brain state activation, they report more diffuse and panoramic attention. Ratings of "stability of attention and intensity of ACAM-J" were also positively correlated with global brain state maximum power and energy values, suggesting that greater activation range of these brain states may be associated with more stable attention and intensity of ACAM-J meditative state experience (Fig. 6A). Interestingly, this differs from phenomenological patterns observed in psychedelic-induced states in which the magnitude of connectome-based eigenmode mean energy was positively correlated with subjective reports of ego dissolution and emotional arousal (Atasoy et al. 2017). Our results showed globally greater mean and total power was negatively correlated with ratings of "late phenomenology of sounds" (ACAM J5 to J6-8; Fig. 6B). Yet, during early

Downloaded from https://academic.oup.com/cercor/article/35/2/bhaf039/8046926 by Harvard Biostatistics user on 04 March 2025

ACAM-J states (ACAM-J1 to J4), ratings of phenomenology were only significantly correlated to the range—rather than total or mean—of brain state power and energy. Specifically, "early phenomenology of sights" and "sounds" were significantly correlated with global brain state maximum power and energy (Fig. 6B). However, it should be noted that further research is needed to explicate the significance between geometric eigenmode activation and behavioral correlations.

Interestingly, ACAM-J2, ACAM-J3, and ACAM-J6-8—where we observed elevated brain state activation across the frequency spectrum but primarily in coarse to moderately fine granular spatial patterns—fall in between pivotal landmarks in ACAM-J progression: ACAM-J1 indicates transition into the form ACAM-J, while ACAM-J4 to ACAM-J5 marks the transition from form to formless ACAM-J. In particular, ACAM-J4—characterized by deep equanimity—has been associated with distinct neural patterns compared to the rest of the ACAM-J in prior studies (Hagerty et al. 2013; Yang et al. 2024a). This suggests that the lack of difference between ACAM-J4 and control tasks we observed may not be subject-specific, though replication with group cohorts is needed. Further research is needed to clarify differences between control cognitions and ACAM-J4, which is a transitory state in deep, formless ACAM-J states of consciousness, if not reflected in the system-wide physiological patterns of geometric eigenmode activation. Trends analysis within ACAM-J further evidence this landmark-specific global brain state activation pattern across the form to formless ACAM-J progression. The positive cubic brain state activation trends for 56 (mean power) and 62 (mean energy) out of 200 eigenmodes indicate a nonlinear relationship between ACAM-J and geometric eigenmode activation (Galante et al. 2023; Yang et al. 2024a). These brain states uniformly peak at ACAM-J that is phenomenologically marked as "bliss and joy" (Brahm 2005; Sayadaw 2008), decreasing through ACAM-J3-J4, reaching a trough at ACAM-J5, marked as the "base of boundless space," before rising through ACAM-J6-8 (Sayadaw 2008; Yang et al. 2024a). This aligns with the previous work of Hagerty et al. (Hagerty et al. 2013) and recently by Yang et al. (Yang et al. 2024a), demonstrating nonlinear trends in brain activation across ACAM-J not only in single regions or networks but also in brain-wide, frequency-specific modes.

In addition to these global metrics, cubic eigenmode trends appear to occur in a frequency-specific manner, occurring primarily in the 50 to 100 eigenmode range (Fig. 6B and E). This range location is mid-spectrum, unlike psychedelic-induced states where brain activity shifts predominately to higher-frequency eigenmodes (Atasoy et al. 2017; Luppi et al. 2023) or anesthesia and brain injury–induced loss of consciousness states where brain activity shifts to deactivation of higher-frequency eigenmodes and activation of lower-frequency eigenmodes (Luppi et al. 2023). Additionally, we observed elevated mean power and energy primarily in eigengroups, of coarse-to-moderately fine granular spatial patterns (low-to-mid-upper eigengroup numbers; Fig. 4). Recall that mid-frequency eigenmodes are coarser-grained spatial patterns where cortical geometry more so constrains the similarity of elements' functional signals compared to high-frequency eigenmodes. Cubic activation trends in eigenmodes in the mid-spectrum range may may reflect the controlled nature of meditation-induced altered perceptions (Sayadaw 2008; Hagerty et al. 2013; Yang et al. 2024a), compared to a more dramatic departure from structural constraints and altered sensations and perceptions seen in pharmacologically induced psychedelic states (Carhart-Harris and Friston 2019). We note that methodological differences, including eigenmode derivation approaches (geometric versus connectome-based) and temporal resolution, limit direct comparisons for some of these differences.

Similarly extending past global power and energy eigenmode trends—compared to non-meditative controls, select ACAM-J show frequency-specific elevation in brain state activation as well. ACAM-J6-8 mean power had a significantly steeper slope compared to the memory control condition, which is similar to results seen in LSD-induced psychedelic states compared to placebo controls (Atasoy et al. 2017). Furthermore, differences in frequency-specific eigengroup mean power and energy were observed in ACAM-J2, ACAM-J3, and ACAM-J6-8 across the 200 eigenmode spectrum. Frequency-specific eigengroup maximum and mean power and energy were also correlated with ratings of "early phenomenology of sights" and "early phenomenology of sounds" in early ACAM-J. The negative association between maximum brain state activation and ratings of phenomenology of "sounds" in eigengroups distributed across both coarse- (low eigengroup) and fine-grain (high eigengroup) spatial scales (eigengroups 1, 5, 8, 10, 11, and 14; Fig. 6C) during ACAM-J1 suggests that the dynamic variability in functional signals that are correlated with decreased sounds sensations are not strongly constrained by cortical geometry. Conversely, the positive association between ratings of "phenomenology of sights" and (i) maximum energy and power of eigengroup 1; (ii) mean power and energy of eigengroups 1, 3, 6, and 9 to 11 in ACAM-J2; and (iii) mean power and energy of eigengroups 10 and 14 in ACAM-J3, implicate recruitment of a distributed range of overlapping spatial patterns in ACAM-J2 and ACAM-J3 associated with ratings of "sights" (Fig. 6D–G). While the positive association between sights sensations and the dynamic variability of eigengroup power and energy is concentrated in large-scale, coarse spatial pattern eigenmodes during ACAM-J2 and ACAM-J3 (maximum power and energy of eigengroup 1), this positive association is observed more broadly across averaged power and energy of moderate and finer-grained spatial patterns during these ACAM-J (mean power and energy of ACAM-J2 eigengroups 1, 3, 6, and 9 to 11; mean power and energy of ACAM-J3 eigengroups 10 and 14).

It has been proposed that through a predictive-processing lens, ACAM-J increases the precision-weighting of a specific source of the current sensory experience, which subsequently reduces (i.e. down-weights) higher-order distracting thoughts and brings the practitioner out of the narrative self (Laukkonen and Slagter 2021). Interestingly, we found that, regardless of eigengroup frequency, brain state activation was only associated with sights and sounds in early states ACAM-J1, ACAM-J2, and ACAM-J3. This progressive decline in external sensory associations may be related to the increasing ACAM-J depth (Gilead et al. 2020; Laukkonen and Slagter 2021). Furthermore, in ACAM-J2, ACAM-J3, and ACAM-J6-8—the states surrounding the form and formless entry points of ACAM-J1 and ACAM-J4/ACAM-J5—we see altered brain state energy distributions indicative of increasingly complex conscious states, such as those observed with use of psychedelics and focused attention meditation (Atasoy et al. 2017; Atasoy et al. 2023). Overall, these results paint a nuanced picture of the neural signatures associated with the ACAM-J progression. These characterizations appear to not only reflect the increase in meditative depth across the early portion of the progression but also how precise, nonlandmark ACAM-J states show a psychedelic-like elevation and expansion of brain state repertoire associated with diffuse, stable attention and increased ACAM-J factor intensity.

This study has strengths including use of ultrahigh resolution 7T fMRI data, rigorous statistical thresholding, and a novel neuroimaging analysis approach. However, there are limitations

Downloaded from https://academic.oup.com/cercor/article/35/2/bhaf039/8046926 by Harvard Biostatistics user on 04 March 2025

to the scope of the experiment methodology used that should be noted, including compromised button press accuracy during heightened absorption of deeper ACAM-J states as well as limited generalizability across different contemplative traditions and meditators, described in Yang et al. (2024a). Additionally, caution should be taken when interpreting and comparing results of geometric-based eigenmodes (derived from the cortical surface via T1 images) and connectome-based eigenmodes (derived from the structural connectome via T1w and DWI). While connectome and geometric eigenmode decomposition methods rest on similar mathematical frameworks, their derivations differ and as do subsequent implications for brain function. While Pang et al. (2023) found higher fMRI resting-state and task based reconstruction accuracy with geometric eigenmode decomposition, subsequent studies using different preprocessing methods and eigenmode generation parameters found comparable (Mansour et al. 2024) or better performance (Vohryzek et al. 2024) with eigenmodes other than those geometrically derived, suggesting that the rare long-range exceptions play a crucial role in time-critical information flow in the human brain (Deco et al. 2021). It would be of significant interest to use these new methods on ACAM-J, which would allow for deeper insights into the links between ACAM-J, other advanced meditation practices, and/or other altered states of consciousness. Moreover, additional investigation should be done on how geometric eigenmodes can be generalized to analysis of subcortical regions, which have simpler (e.g. smoother) geometry compared to the cerebral cortex (Luo et al. 2023). A broader range of eigenmodes may also be tested to look for brain activity trends at higher frequency modes. Interpretations of brain state trends may change depending on the number of eigenmodes extracted. Finally, while extensive sampling of a single subject and event has proven to be a valuable neuroscientific tool that offers insights going beyond those derived from limited repetitions (Levenson et al. 2012; Poldrack et al. 2015), relying on data from a single subject restricts the generalizability of our findings. Interpretations presented here are speculative and need further replication among practitioners from different traditions and expertise levels to expand these findings (Chowdhury et al. 2024; van Lutterveld et al. 2024b). Given the spatial similarity in key functional gradients (which describe the principal axes of spatial organization as captured by similarities in functional connectivity; Margulies et al. 2016) and lower frequency eigenmodes within the subcortex (Pang et al. 2023), a future area of study may be analysis of ACAM-J via gradient analysis. This may elucidate functional reorganization of the brain during advanced concentrative absorption meditation states and allow for comparison with the distributed brain state activation patterns revealed through geometric and connectome eigenmode analysis.

Conclusion

The present study used geometric eigenmode-based decomposition of ultrahigh field-strength fMRI data to explore the characterization of fundamental brain states underlying the complex cortical dynamics of ACAM-J. Notably, using this framework ACAM-J2, ACAM-J3, and ACAM-J6-8 emerged as distinct from non-meditative controls across global spectra analyses, with numerous mid-spectrum eigenmode power and energy exhibiting a nonrandom, cubic trajectory through the form to formless ACAM-J sequence. Correlations with phenomenological ratings suggest that globally elevated brain state activation during meditation is associated with greater ACAM-J intensity and more stable, diffuse attention, as well as stronger sights and weaker sound sensations at the start of ACAM-J. Overall, these results contribute valuable insights into the neural signatures of absorptive and highly concentrative conscious states, revealing a nonrandom, nonlinear trajectory of distributed brain state activation. Our findings underscore the utility of exploring advanced meditative states for wider applicability and to investigate refined conscious states inaccessible in normal conditions.

Author contributions

Ruby M. Potash (Formal analysis, Software, Visualization, Writing—original draft, Writing—review & editing), Winson Fu Zun Yang (Formal analysis, Software, Visualization, Writing—original draft, Writing—review & editing), Brian Winston (Software, Writing—review & editing), Selen Atasoy (Writing—review & editing), Morten Kringelbach (Writing—review & editing), Terje Sparby (Investigation, Methodology, Writing—review & editing), and Matthew D. Sacchet (Conceptualization, Funding acquisition, Investigation, Methodology, Project administration, Resources, Supervision, Writing—original draft, Writing—review & editing).

Supplementary material

Supplementary material is available at *Cerebral Cortex* online.

Supplementary Data 1 and 2 may be found at: https://osf.io/q4cwy/?view_only=8c91ea60b4f14fe3bf8b62e32238c011

Funding

M.D.S. and the Meditation Research Program are supported by the National Institute of Mental Health (Project Number R01MH125850), Dimension Giving Fund, Ad Astra Chandaria Foundation, Brain and Behavior Research Foundation (Grant Number 28972), BIAL Foundation (Grant Number 099/2020), and individual donors. T.S. is supported by Software AG Stiftung. B.W. is supported by the Johns Hopkins Aging and Dementia T32 Predoctoral Training Fellowship funded by the National Institute on Aging and the Johns Hopkins Center for Psychedelic and Consciousness Research.

Conflict of interest statement: None declared.

Data availability

Data may be requested from the corresponding author and subjected to the Mass General Brigham's IRB approval. Code used in this study can be provided upon request from the corresponding author.

Ethics approval statement

The Mass General Brigham IRB approved the study (2019P003902).

Patient approval statement

The participant provided informed consent.

References

Applebaum M. 2019. Remembrance: a husserlian phenomenology of sufi practice. *J Specul Philos*. 33:22–40. https://doi.org/10.5325/jspecphil.33.1.0022.

Downloaded from https://academic.oup.com/cercor/article/35/2/bhaf039/8046926 by Harvard Biostatistics user on 04 March 2025

Atasoy S, Donnelly I, Pearson J. 2016. Human brain networks function in connectome-specific harmonic waves. *Nat Commun*. 7:10340. https://doi.org/10.1038/ncomms10340.

Atasoy S et al. 2017. Connectome-harmonic decomposition of human brain activity reveals dynamical repertoire re-organization under lsd. *Sci Rep*. 7:17661. https://doi.org/10.1038/s41598-017-17546-0.

Atasoy S, Deco G, Kringelbach ML, Pearson J. 2018a. Harmonic brain modes: a unifying framework for linking space and time in brain dynamics. *Neuroscientist*. 24:277–293. https://doi.org/10.1177/1073858417728032.

Atasoy S, Vohryzek J, Deco G, Carhart-Harris RL, Kringelbach ML. 2018b. Common neural signatures of psychedelics: Frequency-specific energy changes and repertoire expansion revealed using connectome-harmonic decomposition. In: Calvey T, editors. *Progress in brain research*. Elsevier; pp. 97–120. https://doi.org/10.1016/bs.pbr.2018.08.009.

Atasoy S et al. 2023. The meditative brain: state and trait changes in harmonic complexity for long-term mindfulness meditators. *bioRxiv202320112016567347*. https://doi.org/10.1038/ncomms10340.

Bates D, Mächler M, Bolker B, Walker S. 2015. Fitting linear mixed-effects models using lme4. *J Stat Softw*. 67:1–48. https://doi.org/10.18637/jss.v067.i01.

Benjamini Y, Hochberg Y. 1995. Controlling the false discovery rate: a practical and powerful approach to multiple testing. *J R Stat Soc Ser B Methodol*. 57:289–300. https://doi.org/10.1111/j.2517-6161.1995.tb02031.x.

Boyes A et al. 2024. Geometric eigenmode brain fingerprinting and its longitudinal associations with adolescent mental health and wellbeing. *bioRxiv202420082008607260*. https://doi.org/10.1111/j.2517-6161.1995.tb02031.x.

Brahm A. 2005. *Mindfulness, bliss, and beyond: a meditator's handbook*. Wisdom Publications Inc.

Buddhaghosa B. 2010. *The path of purification: Visuddhimagga*. Buddhist Pulication Society.

Cao T et al. 2024. Mode-based morphometry: a multiscale approach to mapping human neuroanatomy. *Hum Brain Mapp*. 45:e26640. https://doi.org/10.1002/hbm.26640.

Carhart-Harris RL, Friston KJ. 2019. Rebus and the anarchic brain: toward a unified model of the brain action of psychedelics. *Pharmacol Rev*. 71:316. https://doi.org/10.1124/pr.118.017160.

Catherine S. 2008. *Focused and fearless: a meditator's guide to states of deep joy, calm, and clarity*. Wisdom Publications Inc.

Chen Y-C et al. 2022. The individuality of shape asymmetries of the human cerebral cortex. *elife*. 11:e75056. https://doi.org/10.7554/eLife.75056.

Chowdhury A et al. 2023. Investigation of advanced mindfulness meditation "cessation" experiences using eeg spectral analysis in an intensively sampled case study. *Neuropsychologia*. 190:108694. https://doi.org/10.1016/j.neuropsychologia.2023.108694.

Chowdhury A et al. 2024. Corrigendum: investigation of advanced mindfulness meditation cessation experiences using eeg spectral analysis in an intensively sampled case study. [neuropsychologia (2023) 190, 108694]. *Neuropsychologia*. 203:108972. https://doi.org/10.1016/j.neuropsychologia.2024.108972.

Cox RW. 1996. Afni: software for analysis and visualization of functional magnetic resonance neuroimages. *Comput Biomed Res*. 29:162–173. https://doi.org/10.1006/cbmr.1996.0014.

Deco G et al. 2021. Rare long-range cortical connections enhance human information processing. *Curr Biol*. 31:4436–4448.e4435. https://doi.org/10.1016/j.cub.2021.07.064.

DeLosAngeles D et al. 2016. Electroencephalographic correlates of states of concentrative meditation. *Int J Psychophysiol*. 110:27–39. https://doi.org/10.1016/j.ijpsycho.2016.09.020.

Dennison P. 2019. The human default consciousness and its disruption: insights from an eeg study of buddhist jhāna meditation. *Front Hum Neurosci*. 13. https://doi.org/10.3389/fnhum.2019.00178.

Dor-Ziderman Y, Ataria Y, Fulder S, Goldstein A, Berkovich-Ohana A. 2016. Self-specific processing in the meditating brain: a meg neurophenomenology study. *Neuroscience of Consciousness*. 2016:niw019. https://doi.org/10.1093/nc/niw019.

Ernst CW. 1998. The psychophysiology of ecstasy in sufism and yoga. *N C Med J*. 59:182–184.

Fisher NE. 2022. Flavors of ecstasy: states of absorption in islamic and jewish contemplative traditions. *Religions*. 13:935. https://doi.org/10.3390/rel13100935.

Folstein MF, Folstein SE, McHugh PR. 1975. "mini-mental state". A practical method for grading the cognitive state of patients for the clinician. *J Psychiatr Res*. 12:189–198. https://doi.org/10.1016/0022-3956(75)90026-6.

Friston KJ et al. 2007. *Statistical parametric mapping: the analysis of functional brain images*. Academic Press. https://doi.org/10.1016/B978-012372560-8/50050-4.

Galante J et al. 2023. A framework for the empirical investigation of mindfulness meditative development. *Mindfulness*. 14:1054–1067. https://doi.org/10.1007/s12671-023-02113-8.

Ganesan S, Yang WFZ, Chowdhury A, Zalesky A, Sacchet MD. 2024. Within-subject reliability of brain networks during advanced meditation: an intensively sampled 7 tesla mri case-study. *Hum Brain Mapp*. 45:e26666. https://doi.org/10.1002/hbm.26666.

Gilead M, Liberman N, Trope Y. 2020. Above and beyond the concrete: the diverse representational substrates of the predictive brain. *Behav Brain Sci*. 43:e121. https://doi.org/10.1017/S0140525X19002000.

Glasser MF et al. 2013. The minimal preprocessing pipelines for the human connectome project. *NeuroImage*. 80:105–124. https://doi.org/10.1016/j.neuroimage.2013.04.127.

Glomb K et al. 2021. Functional harmonics reveal multi-dimensional basis functions underlying cortical organization. *Cell Rep*. 36:109554. https://doi.org/10.1016/j.celrep.2021.109554.

Gunaratana H. 1988. *The jhanas in theravada buddhist meditation*. Sri-Lanka: Buddhist Publication Society.

Hagerty MR et al. 2013. Case study of ecstatic meditation: Fmri and eeg evidence of self-stimulating a reward system. *Neural Plasticity*. 2013:653572. https://doi.org/10.1155/2013/653572.

Kuznetsova A, Brockhoff PB, Christensen RHB. 2017. Lmertest package: tests in linear mixed effects models. *J Stat Softw*. 82:1–26. https://doi.org/10.18637/jss.v082.i13.

Laukkonen RE, Slagter HA. 2021. From many to (n)one: meditation and the plasticity of the predictive mind. *Neurosci Biobehav Rev*. 128:199–217. https://doi.org/10.1016/j.neubiorev.2021.06.021.

Laukkonen RE et al. 2023. Cessations of consciousness in meditation: advancing a scientific understanding of nirodha samāpatti. *Prog Brain Res*. 280:61–87. https://doi.org/10.1016/bs.pbr.2022.12.007.

Levenson RW, Ekman P, Ricard M. 2012. Meditation and the startle response: a case study. *Emotion*. 12:650–658. https://doi.org/10.1037/a0027472.

Luo N, Zhang J, Jiang T. 2023. How does brain geometry influence human brain function? *Trends Cogn Sci*. 27:886–887. https://doi.org/10.1016/j.tics.2023.08.005.

Luppi AI et al. 2023. Distributed harmonic patterns of structure-function dependence orchestrate human consciousness.

Downloaded from https://academic.oup.com/cercor/article/35/2/bhaf039/8046926 by Harvard Biostatistics user on 04 March 2025

Communications Biology. 6:117. https://doi.org/10.1038/s42003-023-04474-1.

Luppi AI et al. 2024. Unravelling consciousness and brain function through the lens of time, space, and information. *Trends Neurosci*. 47:551–568. https://doi.org/10.1016/j.tins.2024.05.007.

Mansour LS et al. 2024. Eigenmodes of the brain: revisiting connectomics and geometry. *bioRxiv202420042016589843*.

Margulies DS et al. 2016. Situating the default-mode network along a principal gradient of macroscale cortical organization. *Proc Natl Acad Sci USA*. 113:12574–12579. https://doi.org/10.1073/pnas.1608282113.

Pang JC et al. 2023. Geometric constraints on human brain function. *Nature*. 618:566–574. https://doi.org/10.1038/s41586-023-06098-1.

Poldrack RA et al. 2015. Long-term neural and physiological phenotyping of a single human. *Nat Commun*. 6:8885. https://doi.org/10.1038/ncomms9885.

Preti MG, Van De Ville D. 2019. Decoupling of brain function from structure reveals regional behavioral specialization in humans. *Nat Commun*. 10:4747. https://doi.org/10.1038/s41467-019-12765-7.

Proix T, Perich MG, Milekovic T. 2023. Misinterpreting the horseshoe effect in neuroscience. *bioRxiv202220032004482986*. https://doi.org/10.1101/2022.03.04.482986.

Rasmussen T, Snyder S. 2009. *Practicing the jhanas*. Shambhala Publications.

R-Core-Team. 2023. *R: a language and environment for statistical computing*. 4.3.1 ed. Vienna, Austria: R Core Team.

Rué-Queralt J et al. 2021. Decoding brain states on the intrinsic manifold of human brain dynamics across wakefulness and sleep. *Communications Biology*. 4:854. https://doi.org/10.1038/s42003-021-02369-7.

Sacchet MD, Fava M, Garland EL. 2024. Modulating self-referential processing through meditation and psychedelics: is scientific investigation of self-transcendence clinically relevant. *World Psychiatry*. 23:298–299. https://doi.org/10.1002/wps.21214.

Sayadaw P-AT. 2008. *Knowing and seeing*. Singapore: Pa-Auk Meditation Centre.

Seabold S, Perktold J. 2010. Statsmodels: econometric and statistical modeling with python. Proceedings of the 9th python in science conference. https://doi.org/10.25080/Majora-92bf1922-011.

Sezer I, Pizzagalli DA, Sacchet MD. 2022. Resting-state fmri functional connectivity and mindfulness in clinical and non-clinical contexts: a review and synthesis. *Neurosci Biobehav Rev*. 135:104583. https://doi.org/10.1016/j.neubiorev.2022.104583.

Sheehan DV et al. 1998. The mini-international neuropsychiatric interview (m.I.N.I.): the development and validation of a structured diagnostic psychiatric interview for dsm-iv and icd-10. *J Clin Psychiatry*. 59 Suppl 20:22–33 quiz 34-57.

Shinn M. 2023. Phantom oscillations in principal component analysis. *Proc Natl Acad Sci USA*. 120:e2311420120. https://doi.org/10.1073/pnas.2311420120.

Sparby T. 2019. Phenomenology and contemplative universals: the meditative experience of dhyana, coalescence, or access concentration. *J Conscious Stud*. 26:130–156. https://doi.org/10.1073/pnas.2311420120.

Sparby T, Sacchet MD. 2022. Defining meditation: foundations for an activity-based phenomenological classification system. *Front Psychol*. 12. https://doi.org/10.3389/fpsyg.2021.795077.

Sparby T, Sacchet MD. 2024. Toward a unified account of advanced concentrative absorption meditation. A systematic definition and classification of jhāna. *Mindfulness*. 15:1375–1394. https://doi.org/10.1007/s12671-024-02367-w.

Tang YY, Rothbart MK, Posner MI. 2012. Neural correlates of establishing, maintaining, and switching brain states. *Trends Cogn Sci*. 16:330–337. https://doi.org/10.1016/j.tics.2012.05.001.

Tang Y-Y, Hölzel BK, Posner MI. 2015. The neuroscience of mindfulness meditation. *Nat Rev Neurosci*. 16:213–225. https://doi.org/10.1038/nrn3916.

Trautwein F-M et al. 2024. Suspending the embodied self in meditation attenuates beta oscillations in the posterior medial cortex. *J Neurosci*. 44:e1182232024. https://doi.org/10.1523/JNEUROSCI.1182-23.2024.

Van Dam NT et al. 2018. Mind the hype: a critical evaluation and prescriptive agenda for research on mindfulness and meditation. *Perspect Psychol Sci*. 13:36–61. https://doi.org/10.1177/1745691617709589.

van Lutterveld R, Chowdhury A, Ingram DM, Sacchet MD. 2024a. Neurophenomenological investigation of mindfulness meditation "cessation" experiences using eeg network analysis in an intensively sampled adept meditator. *Brain Topogr*. 37:849–858. https://doi.org/10.1007/s10548-024-01052-4.

van Lutterveld R, Chowdhury A, Ingram DM, Sacchet MD. 2024b. Response to letter to the editors "neurophenomenological investigation of mindfulness meditation "cessation" experiences using eeg network analysis in an intensively sampled adept meditator". *Brain Topogr*. 38:13. https://doi.org/10.1007/s10548-024-01090-y.

Vohryzek J, Kringelbach ML, Deco G. 2024. Beyond cortical geometry: brain dynamics shaped by long-range connections. *bioRxiv202420042009588757*. https://doi.org/10.1101/2024.04.09.588757.

Wright MJ, Sanguinetti JL, Young S, Sacchet MD. 2023. Uniting contemplative theory and scientific investigation: toward a comprehensive model of the mind. *Mindfulness*. 14:1088–1101. https://doi.org/10.1007/s12671-023-02101-y.

Yamashiro J. 2015. Brain basis of samadhi: the neuroscience of meditative absorption. *New Sch Psychol Bull*. 13:1–10. https://doi.org/10.1007/s10548-024-01090-y.

Yang WFZ et al. 2024a. Intensive whole-brain 7t mri case study of volitional control of brain activity in deep absorptive meditation states. *Cereb Cortex*. 34. https://doi.org/10.1093/cercor/bhad408.

Yang WFZ, Sparby T, Wright M, Kim E, Sacchet MD. 2024b. Volitional mental absorption in meditation: toward a scientific understanding of advanced concentrative absorption meditation and the case of jhana. *Heliyon*. 10:e31223. https://doi.org/10.1016/j.heliyon.2024.e31223.

Downloaded from https://academic.oup.com/cercor/article/35/2/bhaf039/8046926 by Harvard Biostatistics user on 04 March 2025

© The Author(s) 2025. Published by Oxford University Press. All rights reserved. For permissions, please e-mail: journals.permission@oup.com.